New scaling measurements map the transition from single-particle to correlated-pair dominance in atomic nuclei

I. Korover,[1,*] A.W. Denniston,[1,*] A. Schmidt,[2] A. Kiral,[1] A. Lovato,[3] N. Rocco,[4] L.B. Weinstein,[5] E. Piasetzky,[6] O. Hen,[1,†] M.J. Amaryan,[5] Giovanni Angelini,[2] H. Atac,[7] N.A. Baltzell,[8] L. Barion,[9] M. Battaglieri,[8,10] I. Bedlinskiy,[11] Fatiha Benmokhtar,[12] A. Bianconi,[13,14] L. Biondo,[10,15,16] A.S. Biselli,[17,18] F. Bossù,[19] S. Boiarinov,[8] W.J. Briscoe,[2] D. Bulumulla,[5] V.D. Burkert,[8] D.S. Carman,[8] J.C. Carvajal,[20] M. Caudron,[21] P. Chatagnon,[21] T. Chetry,[22] G. Ciullo,[9,23] L. Clark,[24] P.L. Cole,[25,26,8] M. Contalbrigo,[9] G. Costantini,[13,14] A. D'Angelo,[27,28] N. Dashyan,[29] R. De Vita,[10] M. Defurne,[19] A. Deur,[8] S. Diehl,[30,31] C. Djalali,[32] R. Dupre,[21] H. Egiyan,[8] M. Ehrhart,[3] A. El Alaoui,[33] L. El Fassi,[22] L. Elouadrhiri,[8] P. Eugenio,[34] S. Fegan,[35] R. Fersch,[36] A. Filippi,[37] G. Gavalian,[8,38] Y. Ghandilyan,[29] G.P. Gilfoyle,[39] F.X. Girod,[8] A.A. Golubenko,[40] R.W. Gothe,[41] K.A. Griffioen,[42] M. Guidal,[21] L. Guo,[20,8] K. Hafidi,[3] H. Hakobyan,[33,29] M. Hattawy,[5] T.B. Hayward,[31] D. Heddle,[36,8] K. Hicks,[32] A. Hobart,[21] M. Holtrop,[38] C.E. Hyde,[5] Y. Ilieva,[41,2] D.G. Ireland,[24] E.L. Isupov,[40] H.S. Jo,[43] K. Joo,[31] S. Joosten,[3] D. Keller,[44] A. Khanal,[20] M. Khandaker,[45,‡] A. Kim,[31] W. Kim,[43] A. Kripko,[30] V. Kubarovsky,[8,46] L. Lanza,[27] M. Leali,[13,14] P. Lenisa,[9,23] K. Livingston,[24] I .J .D. MacGregor,[24] D. Marchand,[21] L. Marsicano,[10] V. Mascagna,[47,14,§] B. McKinnon,[24] S. Migliorati,[13,14] M. Mirazita,[48] V. Mokeev,[8,40] C. Munoz Camacho,[21] P. Nadel-Turonski,[8] K. Neupane,[41] S. Niccolai,[21] G. Niculescu,[49] T. R. O'Connell,[31] M. Osipenko,[10] A.I. Ostrovidov,[34] P. Pandey,[5] M. Paolone,[50] L.L. Pappalardo,[9,23] R. Paremuzyan,[8] E. Pasyuk,[8] O. Pogorelko,[11] M. Pokhrel,[5] J. Poudel,[5] J.W. Price,[51] Y. Prok,[5,44] B.A. Raue,[20,8] Trevor Reed,[20] M. Ripani,[10] J. Ritman,[52] A. Rizzo,[27,28] G. Rosner,[24] P. Rossi,[8] J. Rowley,[32] F. Sabatié,[19] R.A. Schumacher,[18] E.P. Segarra,[1] Y.G. Sharabian,[8] E.V. Shirokov,[40] U. Shrestha,[31] O. Soto,[48] N. Sparveris,[7] S. Stepanyan,[8] I.I. Strakovsky,[2] S. Strauch,[41,2] R. Tyson,[24] M. Ungaro,[8,46] L. Venturelli,[13,14] H. Voskanyan,[29] A. Vossen,[53,8] E. Voutier,[21] Kevin Wei,[31] X. Wei,[8] R. Wishart,[24] M.H. Wood,[54,41] B. Yale,[42] N. Zachariou,[35] J. Zhang,[44] and Z.W. Zhao[53]

(The CLAS Collaboration)

[1] *Massachusetts Institute of Technology, Cambridge, Massachusetts 02139, USA*
[2] *The George Washington University, Washington DC 20052, USA*
[3] *Argonne National Laboratory, Argonne, Illinois 60439*
[4] *Theoretical Physics Department, Fermi National Accelerator Laboratory, P.O. Box 500, Batavia, Illinois 60510, USA*
[5] *Old Dominion University, Norfolk, Virginia 23529*
[6] *School of Physics and Astronomy, Tel Aviv University, Tel Aviv 69978, Israel*
[7] *Temple University, Philadelphia, PA 19122*
[8] *Thomas Jefferson National Accelerator Facility, Newport News, Virginia 23606*
[9] *INFN, Sezione di Ferrara, 44100 Ferrara, Italy*
[10] *INFN, Sezione di Genova, 16146 Genova, Italy*
[11] *National Research Centre Kurchatov Institute - ITEP, Moscow, 117259, Russia*
[12] *Duquesne University, 600 Forbes Avenue, Pittsburgh, PA 15282*
[13] *Università degli Studi di Brescia, 25123 Brescia, Italy*
[14] *INFN, Sezione di Pavia, 27100 Pavia, Italy*
[15] *INFN, Sezione di Catania, 95123 Catania, Italy*
[16] *Universit'a degli Studi di Messina, 98166 Messina, Italy*
[17] *Fairfield University, Fairfield CT 06824*
[18] *Carnegie Mellon University, Pittsburgh, Pennsylvania 15213*
[19] *IRFU, CEA, Université Paris-Saclay, F-91191 Gif-sur-Yvette, France*
[20] *Florida International University, Miami, Florida 33199*
[21] *Universit'e Paris-Saclay, CNRS/IN2P3, IJCLab, 91405 Orsay, France*
[22] *Mississippi State University, Mississippi State, MS 39762-5167*
[23] *Universita' di Ferrara , 44121 Ferrara, Italy*
[24] *University of Glasgow, Glasgow G12 8QQ, United Kingdom*
[25] *Lamar University, 4400 MLK Blvd, PO Box 10046, Beaumont, Texas 77710*
[26] *Catholic University of America, Washington, D.C. 20064*
[27] *INFN, Sezione di Roma Tor Vergata, 00133 Rome, Italy*
[28] *Universita' di Roma Tor Vergata, 00133 Rome Italy*
[29] *Yerevan Physics Institute, 375036 Yerevan, Armenia*
[30] *II Physikalisches Institut der Universitaet Giessen, 35392 Giessen, Germany*
[31] *University of Connecticut, Storrs, Connecticut 06269*
[32] *Ohio University, Athens, Ohio 45701*

[33] Universidad Técnica Federico Santa María, Casilla 110-V Valparaíso, Chile
[34] Florida State University, Tallahassee, Florida 32306
[35] University of York, York YO10 5DD, United Kingdom
[36] Christopher Newport University, Newport News, Virginia 23606
[37] INFN, Sezione di Torino, 10125 Torino, Italy
[38] University of New Hampshire, Durham, New Hampshire 03824-3568
[39] University of Richmond, Richmond, Virginia 23173
[40] Skobeltsyn Institute of Nuclear Physics, Lomonosov Moscow State University, 119234 Moscow, Russia
[41] University of South Carolina, Columbia, South Carolina 29208
[42] College of William and Mary, Williamsburg, Virginia 23187-8795
[43] Kyungpook National University, Daegu 41566, Republic of Korea
[44] University of Virginia, Charlottesville, Virginia 22901
[45] Norfolk State University, Norfolk, Virginia 23504
[46] Rensselaer Polytechnic Institute, Troy, New York 12180-3590
[47] Università degli Studi dell'Insubria, 22100 Como, Italy
[48] INFN, Laboratori Nazionali di Frascati, 00044 Frascati, Italy
[49] James Madison University, Harrisonburg, Virginia 22807
[50] New Mexico State University, PO Box 30001, Las Cruces, NM 88003, USA
[51] California State University, Dominguez Hills, Carson, CA 90747
[52] Institute fur Kernphysik (Juelich), Juelich, Germany
[53] Duke University, Durham, North Carolina 27708-0305
[54] Canisius College, Buffalo, NY

Atomic nuclei are one of the most complex quantum-mechanical systems in nature. Their structure and properties are determined by the many-body interactions among their constituent nucleons (protons and neutrons). While exact calculations of these are highly challenging, they are fundamental for our understanding of phenomena such as astrophysical element production. Physicists thus often model nuclei using divide-and-conquer algorithms that split nuclear interactions into three main domains [1]: Below the nuclear Fermi momentum, nucleons are well modeled as independent particles moving in an average mean field [2–4]; above it, they are predominantly part of strongly interacting short-range correlated pairs [5–7]; in between these domains - near the Fermi level - independent particles, short-range correlated pairs, and low-energy many-body nucleon correlations all contribute [1]. Quantifying this transition region is an outstanding challenge. Here we show a new kind of scaling in the electron-scattering cross section ratio of nuclei relative to deuterium, and map its onset as a function of the initial momentum of the struck proton. We find good agreement with independent particle calculations up to almost the Fermi momentum (∼220 MeV/c) and correlated-pair dominance above 300 MeV/c. Our data support the use of the divide-and-conquer approach to factorize the many-body nuclear wave function into three momentum domains: below, near, and above the Fermi level [6, 8–10]. This factorization, in turn, can allow the construction of precise effective nuclear wave functions and spectral functions that can improve our understanding of the fundamental structure of matter [11, 12], and neutrino-nucleus interactions for precision neutrino oscillation measurements [13].

Traditional models of nuclei simplify the calculation of nuclear wave functions by averaging over the effects of the individual nucleon-nucleon (NN) interactions to determine effective single-nucleon mean-field potentials. These models give rise to nuclear shell-model states, e.g. *s*-, *p*-, *d*-, ... shells. The typical nucleon momenta in each shell is smaller than the nuclear Fermi momentum (k_F).

Full shell-model calculations improve on this by introducing an additional momentum regime that accounts for effective low-energy, many-body, long-ranged correlations around k_F, such as pairing and particle-vibration coupling [1].

While successfully modeling the long-range structure of nuclei, the shell model does not describe the explicit effects of short-range correlated (SRC) nucleon pairs. These arise when two nucleons get so close to each other that the short-range NN interaction becomes much larger than the effective long-ranged nuclear mean field [5–7, 14]. Nucleons in SRC pairs have high (greater than k_F) relative momentum. Their formation depletes the occupancy of shell-model states and introduces a high-momentum "tail" ($k > k_F$) to the nuclear momentum distribution that can account for up to 20% of the nucleons in the nucleus [6, 7, 14–16]. Since the short-range NN interaction is nucleus-independent, the properties of SRC pairs are universal, i.e., largely the same for all nuclei [6, 10].

A complete high-resolution microscopic description of atomic nuclei should therefore go beyond the long-ranged nuclear shell model and also account for the explicit effects of short-range correlations. Effective theoretical models of nuclei can do this by combining nucleus-dependent shell-model momentum distributions with the universal properties of SRC pairs [6, 17–19]. Such models describe well the high- and low-momentum regimes (and the equivalent short- and long-ranged regimes) of the many-body nuclear distribution [10, 20]. However, the transition region between the two regimes is still not well understood, which limits our ability to fully describe the nucleus.

Here, we mapped the mean-field to SRC transition using new measurements of high-energy electron scattering, where we detect the knocked-out proton in addition to the scattered electron. For the first time, we observed scaling over a broad kinematical range in the cross section ratios of nuclei from carbon to lead relative to deuterium. By accounting for the single-nucleon mean-field contributions to this ratio, we isolated the SRC response function and observed a narrow mean-field to SRC transition region, centered slightly above k_F. The narrowness of this transition constrains the contribution of many-body long-range correlations and enables the effective high-resolution description of nuclei using nucleus-dependent low-energy models supplemented by universal high-momentum SRCs.

Our experiment ran at the Thomas Jefferson National Accelerator Facility. It used a 5.01 GeV electron beam incident on a target system consisting of a deuterium cell followed by an interchangeable solid foil of carbon (C), aluminum (Al), iron (Fe), or lead (Pb) [21]. Scattered electrons and knocked-out protons were identified and measured using the CEBAF Large Acceptance Spectrometer (CLAS) [22] (see Methods for details).

In high-energy scattering, the electron transfers a single virtual photon to the nucleus with momentum $\vec{q}$ and energy ω. In the high-resolution quasielastic (QE) reaction picture, the virtual photon is absorbed by a single nucleon, which gets knocked-out of the nucleus with momentum $\vec{p}_p$. By measuring both the scattered electron and knocked-out proton, i.e. the $(e, e'p)$ reaction, we can determine the missing momentum $\vec{p}_{miss} = \vec{p}_p - \vec{q}$.

If the knocked-out nucleon does not re-interact as it leaves the nucleus, $\vec{p}_{miss}$ is equal to the initial momentum of that nucleon. Thus we expect the reaction to be sensitive to mean-field nucleons at low-p_{miss} and to SRCs at high-p_{miss} [23]. In the SRC dominated region, the cross section ratio for any two nuclei should be constant (i.e., independent of p_{miss}) and equal to the relative number of high-momentum nucleons in the two nuclei [6, 7, 15, 17, 24–26]. Thus, by measuring the $(e, e'p)$ cross section ratio for nuclei relative to deuterium for different minimum p_{miss}, we can establish the onset of scaling that corresponds to SRC pair dominance in the nuclear momentum distribution.

To study this, we measured the $(e, e'p)$ reaction in conditions sensitive to the knockout of protons from SRC pairs. We required four-momentum transfer squared $Q^2 = \vec{q}^2 - \omega^2 \geq 1.5$ (GeV/c)^2 and $350 \leq p_{miss} \leq 600$ MeV/c to resolve single nucleons in SRC pairs, and required that the proton be emitted within 25° of the momentum transfer, to ensure that the measured proton was the nucleon that absorbed the virtual photon [27, 28].

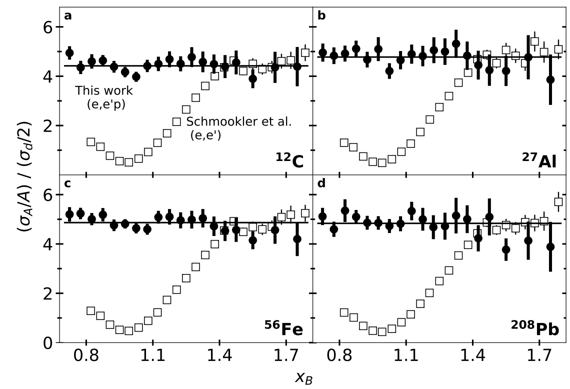

Fig. 1. | Cross section scaling for nuclei from carbon to lead. Measured semi-exclusive $(e, e'p)$ per nucleon cross section ratios for carbon (a), aluminum (b), iron (c) and lead (d) relative to deuterium shown as function of x_B and for $350 \leq p_{miss} \leq 600$ MeV/c. Open squares are the previously measured inclusive (e, e') per nucleon cross section ratios of Ref. [26]. The horizontal lines show the average (e, e') cross section ratio for $1.45 \leq x_B \leq 1.8$ [26]. Error bars show the data uncertainty (statistical plus point-to-point systematical) at the 1σ or 68% confidence level. Overall $(e, e'p)$ systematic uncertainties of 10% (C) to 15% (Pb) are not shown.

We then suppressed inelastic (non-QE) scattering events using M_{miss}, the missing mass for $(e, e'p)$ scattering from a two-nucleon pair at rest, and $\theta_{\vec{p}_{miss},\vec{q}}$, the angle between $\vec{p}_{miss}$ and $\vec{q}$. The $\theta_{\vec{p}_{miss},\vec{q}}$ distribution had two maxima, corresponding to QE and non-QE scattering. In non-QE reactions the momentum transferred to undetected particles (e.g., pions) shifts the direction of $\vec{p}_{miss}$ and increases $\theta_{\vec{p}_{miss},\vec{q}}$. Unlike the M_{miss} distribution, the $\theta_{\vec{p}_{miss},\vec{q}}$ distribution was well fitted with two Gaussians. We required $0.8 \leq M_{miss} \leq m + m_\pi = 1.08$ GeV/c^2 (where m_π is the pion mass) and for each bin in x_B, selected events in the $\theta_{\vec{p}_{miss},\vec{q}}$ QE peak. See Extended Data Figs. 1 and 2 and Methods for details.

We confirmed our identification of scattering from protons in SRC pairs by comparing the measured width of the M_{miss} peak with that calculated using the Generalized Contact Formalism (GCF) [10, 20, 28–31], which assumes electron scattering from nucleons in SRC pairs. The calculation accounted for the CLAS detector acceptance and resolution and our event selection criteria. The data and calculation agree well. See Extended Data Fig. 3 and Methods for details.

Using the selected event samples, we extracted the $(e, e'p)$ cross section ratios for scattering off the solid

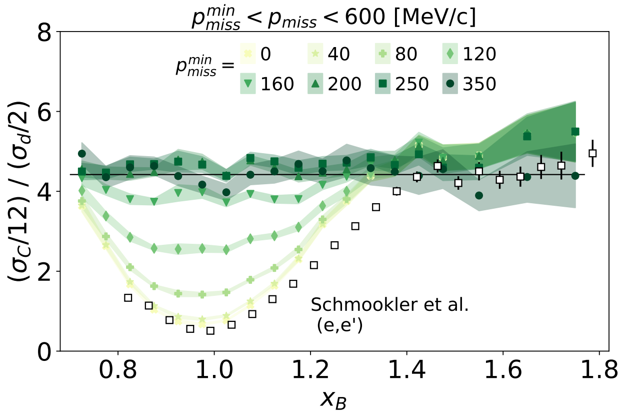

Fig. 2. | Scaling development in carbon to deuterium $(e, e'p)$ cross section ratios. The per-nucleon cross section ratios for carbon to deuterium as a function of x_B. Full symbols with different colors stand for different lower limits of the missing momentum integration. The upper missing momentum limit is fixed at 600 MeV/c. The colored bands mark the statistical plus point-to-point systematical uncertainty of the data at the $\pm 1\sigma$ or 68% confidence level. Overall systematic uncertainties of 10% are not shown. Open squares are the previously measured inclusive (e, e') per nucleon cross section ratios of Ref. [26]. The horizontal line shows the average (e, e') cross section ratio for $1.45 \leq x_B \leq 1.8$ [26].

targets relative to deuterium. We first divided the ratio of the measured numbers of events for a given target to deuterium with the ratio of the experimentally determined integrated luminosities to obtain the normalized-yield ratios. We then determined the cross section ratios by correcting the normalized-yield ratios for attenuation of the outgoing protons as they traverse the different nuclei, and for other experimental effects. These include electron radiation effects and the small difference in the CLAS acceptance for detecting particles emitted from the deuterium and the solid targets. Acceptance effects were calculated using the CLAS detector simulation [32] and an electron scattering reaction event generator based on the GCF as applied in previous studies [28, 30] (see Methods for details).

Figure 1 shows the per nucleon $(e, e'p)$ cross section ratios for $350 \leq p_{miss} \leq 600$ MeV/c for carbon, aluminum, iron, and lead relative to deuterium as a function of the Bjorken scaling variable $x_B = Q^2/2m\omega$ (where m is the nucleon mass). The $(e, e'p)$ ratios scale (i.e., are constant) for all four nuclei over the entire measured x_B range. This implies that the reaction is probing similar nuclear configurations in the measured nuclei and deuterium. As the deuteron is a simple correlated two-body system, we interpret this high missing-momentum scaling as observation of deuteron-like SRC pairs in nuclei. The cross section ratio thus measures their relative abundance.

This interpretation is supported by the consistency between our measured $(e, e'p)$ cross section ratios and previously measured inclusive (e, e') scattering cross section ratios at similar Q^2 and $x_B \geq 1.5$ [15, 17, 24–26]. As the inclusive scaling onset at $x_B \approx 1.5$ has been attributed to scattering off nucleons with momenta greater than ~ 275 MeV/c [15], it is also associated with scattering off nucleons in deuteron-like SRC pairs [17, 26] (see Methods for details). Proton detection extends the $(e, e'p)$ cross section ratio plateau down to $x_B = 0.7$, providing a new tool to study the transition to SRC dominance in nuclei.

To this end, we examined how this scaling depends on the minimum p_{miss}. Figure 2 shows the per nucleon $(e, e'p)$ cross section ratios for carbon relative to deuterium as a function of x_B for different minimum p_{miss}. The curve for $p_{miss}^{min} = 0$ agrees reasonably well with the inclusive data of Schmookler et al. [26], with a minimum at $x_B \approx 1$ and a plateau for $x_B \geq 1.5$. As p_{miss}^{min} increases, this minimum fills in. For $p_{miss}^{min} \geq 200$ MeV/c, it is completely filled in and the $(e, e'p)$ cross section ratio scales over the full measured x_B range of 0.7 to 1.8. This indicates that short-range interactions become dominant at around $k_F \approx 220$ MeV/c, as expected. Results for other nuclei are shown in Extended Data Fig. 4.

To better quantify this transition, we study the carbon to deuterium $(e, e'p)$ cross section ratio integrated over $0.7 \leq x_B \leq 1.8$ as a function of p_{miss}, as shown in Fig. 3(a) (and Extended Data Fig. 5 for other nuclei). The high-p_{miss} data are in excellent agreement with a GCF calculation whose parameters were fully determined by $ab-initio$ many-body calculations [10]. This agreement further supports our identification of QE scattering events and the dominance of scattering from nucleons in SRC pairs at high-p_{miss}.

The cross section ratio becomes flat starting at $p_{miss} \approx 250$ MeV/c for all nuclei except lead. Lead also has a transition at $p_{miss} \approx 250$ MeV/c, but the ratio does not then become completely flat, possibly because it has a much larger neutron-to-proton ratio and because its larger mass and size might increase the effects of final state interactions. This 250 MeV/c transition point is slightly larger than the extracted carbon Fermi momentum, $k_F = 220$ MeV/c [33].

We quantified the transition by subtracting the contribution of interactions with the mean-field nucleons in carbon from the total measured cross section ratio. We calculated this contribution using a factorized plane-wave impulse approximation with mean-field spectral functions extracted from Quantum Monte-Carlo (QMC) calculations of the overlap between the ^{12}C and ^{11}B+proton wave functions (see Methods for details). We added the contributions from the ground state and a range of ^{11}B excited states to include a wide range of mean-field, single-nucleon states. The ratio of this C$(e, e'p)$ mean-field-only calculation to the calculated deuterium cross section agrees well with the measured cross section ra-

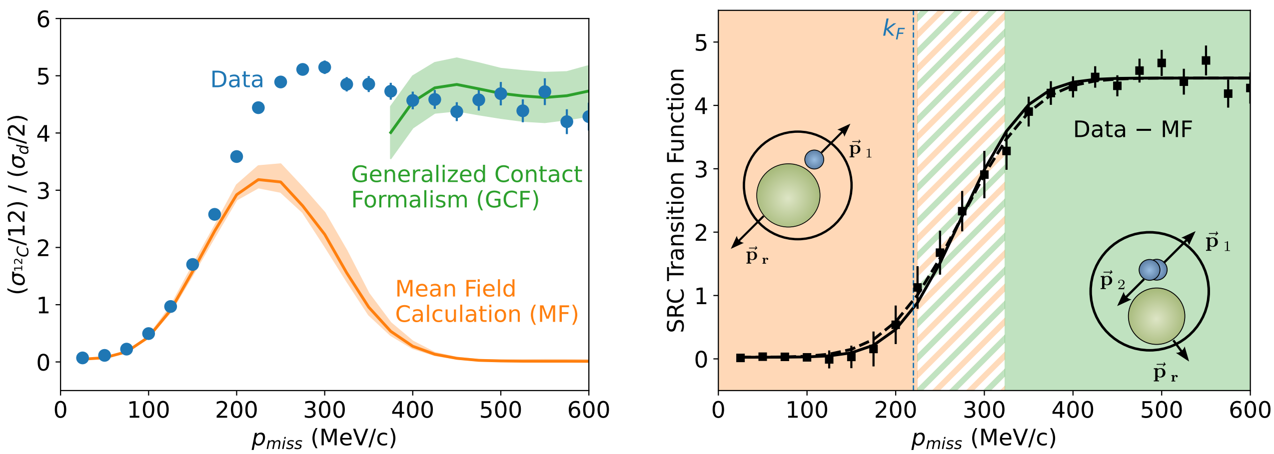

Fig. 3. | **Mean field to SRC transition.** (left) The per nucleon $(e, e'p)$ cross section ratios for carbon to deuteron as a function of p_{miss}, integrated over $0.7 \le x_B \le 1.8$. The filled blue circles show the data; the orange and green lines show the ratios of the calculated cross sections for mean-field and SRC nucleons in carbon, respectively, divided by the calculated deuterium cross section. Data error bars and the widths of the bands show their uncertainties (statistical plus point-to-point systematical) at the 1σ or 68% confidence level. Overall data systematic uncertainties of 10% are not shown. (right) SRC transition function (black squares) defined as the difference between the measured cross section ratios and the mean-field calculation (labelled "Data - MF"). The dashed black line is the result of an Error function fit to the points and the solid black line shows the same function with a narrower width after accounting for the effect of the CLAS detector resolution. The orange region corresponds to the low-momentum mean-field region, the green region to the high-momentum SRC region, and the hatched region between them shows the location and width of the transition region from 20% to 80% of the fit function. The vertical dashed blue line indicates the carbon Fermi momentum of 220 MeV/c.

tios up to $p_{miss} \approx 180$ MeV/c (see Fig. 3(a)).

Unlike traditional effective mean-field calculations, here we first compute the fully correlated high-resolution nuclear wave function, and then extract from it the underlying single-nucleon states. Therefore, our carbon spectral function has fewer than six protons in its mean-field orbitals, due to single-nucleon strength lost to long- and short-ranged correlations. Its agreement with our low-p_{miss} data is an experimental confirmation of the QMC calculated integral correlation strength. Due to its complexity, this exact calculation is currently computationally impractical for nuclei heavier than carbon.

Next we subtracted the mean-field contribution (with its associated uncertainties) from the measured cross section ratio to isolate the contribution from non-mean-field protons. As seen in Fig. 3(b), the subtracted cross section ratio matches the profile of a transition function that is zero at low-p_{miss}, starts to grow around k_F, and then saturates at high-p_{miss}. If the nucleus included only mean-field and SRC components, then the transition would be a step function. The existence of long-range correlations leads to a finite width.

This is the first measurement of the width of the mean field to SRC transition. We quantified it by fitting the subtracted data to an Error function (erf). The fitted transition mean was obtained to be 274 ± 3 MeV/c, which is significantly higher than the measured carbon Fermi momentum of 220 MeV/c [33]. The transition width was determined to be 65 ± 4 MeV/c. Subtracting the contribution of the CLAS resolution to the measured width results in an intrinsic width of 58 ± 4 MeV/c. The width of the transition indicates that the overlap region where both long-range and short-range dynamics contribute is narrow.

Thus, the nuclear scaling measurements we present allow isolating interactions with SRC pairs in a new kinematical regime. By examining the scaling onset and accounting for the mean-field contributions to the data we identified a new transition function. This function describes the transition from the mean-field to the SRC components of the nucleus. The narrow nature of the transition enables the use of scale-separated models for calculations of nuclear structure and reactions. This allows a high-resolution description of a wide range of heavy nuclei that are outside the reach of modern numerical ab-initio calculations.

* Equal Contribution
† Contact Author (hen@mit.edu)
‡ Current address:Idaho State University, Pocatello, Idaho 83209
§ Current address:Università degli Studi di Brescia, 25123 Brescia, Italy

[1] W. H. Dickhoff and C. Barbieri. Selfconsistent Green's

function method for nuclei and nuclear matter. *Prog. Part. Nucl. Phys.*, 52:377–496, 2004.

[2] B. Alex Brown and B. H. Wildenthal. Status of the nuclear shell model. *Ann. Rev. Nucl. Part. Sci.*, 38:29–66, 1988.

[3] Gerhard Jacob and Th.A.J. Maris. Quasi-Free Scattering and Nuclear Structure. *Rev. Mod. Phys.*, 38:121–142, 1966.

[4] E. Caurier, G. Martinez-Pinedo, F. Nowacki, A. Poves, and A. P. Zuker. The Shell Model as Unified View of Nuclear Structure. *Rev. Mod. Phys.*, 77:427–488, 2005.

[5] R. Subedi et al. Probing Cold Dense Nuclear Matter. *Science*, 320:1476–1478, 2008.

[6] Claudio Ciofi degli Atti. In-medium short-range dynamics of nucleons: Recent theoretical and experimental advances. *Phys. Rept.*, 590:1–85, 2015.

[7] O. Hen, G. A. Miller, E. Piasetzky, and L. B. Weinstein. Nucleon-Nucleon Correlations, Short-lived Excitations, and the Quarks Within. *Rev. Mod. Phys.*, 89(4):045002, 2017.

[8] Claudio Ciofi degli Atti and S. Simula. Realistic model of the nucleon spectral function in few and many nucleon systems. *Phys. Rev. C*, 53:1689, 1996.

[9] H. Feldmeier, W. Horiuchi, T. Neff, and Y. Suzuki. Universality of short-range nucleon-nucleon correlations. *Phys. Rev. C*, 84:054003, 2011.

[10] R. Cruz-Torres, D. Lonardoni, R. Weiss, N. Barnea, D. W. Higinbotham, E. Piasetzky, A. Schmidt, L. B. Weinstein, R. B. Wiringa, and O. Hen. Many-Body Factorization and Position-Momentum Equivalence of Nuclear Short-Range Correlations. *Nature Physics*, 17:306, 2020.

[11] E. P. Segarra, J. R. Pybus, F. Hauenstein, D. W. Higinbotham, G. A. Miller, E. Piasetzky, A. Schmidt, M. Strikman, L. B. Weinstein, and O. Hen. Short-Range Correlations and the Nuclear EMC Effect in Deuterium and Helium-3. 6 2020.

[12] R. Abdul Khalek et al. Science Requirements and Detector Concepts for the Electron-Ion Collider: EIC Yellow Report. 3 2021.

[13] L. Alvarez-Ruso et al. NuSTEC White Paper: Status and challenges of neutrino–nucleus scattering. *Prog. Part. Nucl. Phys.*, 100:1–68, 2018.

[14] Leonid Frankfurt and Mark Strikman. Hard nuclear processes and microscopic nuclear structure. *Phys. Rep.*, 160(5-6):235 – 427, 1988.

[15] K. Egiyan et al. Measurement of 2- and 3-nucleon short range correlation probabilities in nuclei. *Phys. Rev. Lett.*, 96:082501, 2006.

[16] S. Paschalis, M. Petri, A. O. Macchiavelli, O. Hen, and E. Piasetzky. Nucleon-nucleon correlations and the single-particle strength in atomic nuclei. *Phys. Lett. B*, 800:135110, 2020.

[17] L.L. Frankfurt, M.I. Strikman, D.B. Day, and M. Sargsyan. Evidence for short-range correlations from high q2 (e,e') reactions. *Phys. Rev. C*, 48:2451, 1993.

[18] Or Hen, Bao-An Li, Wen-Jun Guo, L. B. Weinstein, and Eli Piasetzky. Symmetry energy of nucleonic matter with tensor correlations. *Phys. Rev. C*, 91:025803, Feb 2015.

[19] Reynier Cruz-Torres, Axel Schmidt, Gerald A. Miller, Lawrence B. Weinstein, Nir Barnea, Ronen Weiss, Eliezer Piasetzky, and O. Hen. Short range correlations and the isospin dependence of nuclear correlation functions. *Phys. Lett.*, B785:304–308, 2018.

[20] R. Weiss, R. Cruz-Torres, N. Barnea, E. Piasetzky, and O. Hen. The nuclear contacts and short range correlations in nuclei. *Phys. Lett. B*, 780:211, 2018.

[21] H. Hakobyan et al. A double-target system for precision measurements of nuclear medium effects. *Nucl. Instrum. Meth.*, A592:218–223, 2008.

[22] B. A. Mecking et al. The CEBAF Large Acceptance Spectrometer (CLAS). *Nucl. Instrum. Meth.*, A503:513–553, 2003.

[23] M. Duer et al. Probing high-momentum protons and neutrons in neutron-rich nuclei. *Nature*, 560(7720):617–621, 2018.

[24] K. Egiyan et al. *Phys. Rev. C*, 68:014313, 2003.

[25] N. Fomin et al. New measurements of high-momentum nucleons and short-range structures in nuclei. *Phys. Rev. Lett.*, 108:092502, 2012.

[26] B. Schmookler et al. Modified structure of protons and neutrons in correlated pairs. *Nature*, 566(7744):354–358, 2019.

[27] O. Hen et al. Momentum sharing in imbalanced Fermi systems. *Science*, 346:614–617, 2014.

[28] A. Schmidt et al. Probing the core of the strong nuclear interaction. *Nature*, 578(7796):540–544, 2020.

[29] Ronen Weiss, Betzalel Bazak, and Nir Barnea. Generalized nuclear contacts and momentum distributions. *Phys. Rev.*, C92(5):054311, 2015.

[30] J.R. Pybus, I. Korover, R. Weiss, A. Schmidt, N. Barnea, D.W. Higinbotham, E. Piasetzky, M. Strikman, L.B. Weinstein, and O. Hen. Generalized contact formalism analysis of the $^4\text{He}(e,e'pN)$ reaction. *Phys. Lett. B*, 805:135429, 2020.

[31] M. Patsyuk et al. Unperturbed inverse kinematics nucleon knockout measurements with a 48 GeV/c carbon beam. 2 2021.

[32] Elliott Wolin. Clas - geant simulation, 1996.

[33] E. J. Moniz, I. Sick, R. R. Whitney, J. R. Ficenec, R. D. Kephart, and W. P. Trower. Nuclear fermi momenta from quasielastic electron scattering. *Phys. Rev. Lett.*, 26:445–448, Feb 1971.

[34] R. Shneor et al. Investigation of proton-proton short-range correlations via the C-12(e, e-prime pp) reaction. *Phys. Rev. Lett.*, 99:072501, 2007.

[35] E. O. Cohen et al. Center of Mass Motion of Short-Range Correlated Nucleon Pairs studied via the $A(e,e'pp)$ Reaction. *Phys. Rev. Lett.*, 121(9):092501, 2018.

[36] R. Ent, B. W. Filippone, N. C. R. Makins, R. G. Milner, T. G. O'Neill, and D. A. Wasson. Radiative corrections for (e, e-prime p) reactions at GeV energies. *Phys. Rev.*, C64:054610, 2001.

[37] Andreas Aste, Kai Hencken, Jurg Jourdan, Ingo Sick, and Dirk Trautmann. Coulomb corrections for quasielastic (e, e-prime) scattering: Eikonal approximation. *Nucl. Phys.*, A743:259–282, 2004.

[38] J.J. Kelly. Nucleon knockout by intermediate-energy electrons. *Adv. Nucl. Phys.*, 23:75–294, 1996.

[39] R. B. Wiringa, V. G. J. Stoks, and R. Schiavilla. Accurate nucleon-nucleon potential with charge-independence breaking. *Phys. Rev. C*, 51:38–51, Jan 1995.

[40] https://www.phy.anl.gov/theory/research/overlaps/.

[41] J. Carlson, S. Gandolfi, F. Pederiva, Steven C. Pieper, R. Schiavilla, K. E. Schmidt, and R. B. Wiringa. Quantum Monte Carlo methods for nuclear physics. *Rev. Mod. Phys.*, 87:1067, 2015.

[42] D. Dutta et al. A Study of the quasielastic (e,e-prime

p) reaction on C-12, Fe-56 and Au-97. *Phys. Rev. C*, 68:064603, 2003.

[43] R. Weiss, A. W. Denniston, J. R. Pybus, O. Hen, E. Piasetzky, A. Schmidt, L. B. Weinstein, and N. Barnea. Extracting the number of short-range correlated nucleon pairs from inclusive electron scattering data. *Phys. Rev. C*, 103(3):L031301, 2021.

Acknowledgments We acknowledge the efforts of the staff of the Accelerator and Physics Divisions at Jefferson Lab that made this experiment possible. The analysis presented here was carried out as part of the Jefferson Lab Hall B data-mining project supported by the U.S. Department of Energy (DOE). The research was also supported by the National Science Foundation, the Israel Science Foundation, the Pazi Foundation, the Chilean Comisión Nacional de Investigación Científica y Tecnológica, the French Centre National de la Recherche Scientifique and Commissariat a l'Energie Atomique, the French–American Cultural Exchange, the Italian Istituto Nazionale di Fisica Nucleare, the National Research Foundation of Korea, and the UK Science and Technology Facilities Council. Jefferson Science Associates operates the Thomas Jefferson National Accelerator Facility for the DOE, Office of Science, Office of Nuclear Physics under contract DE-AC05-06OR23177.

Author Contributions The CEBAF Large Acceptance Spectrometer was designed and constructed by the CLAS Collaboration and Jefferson Lab. Data acquisition, processing and calibration, Monte Carlo simulations of the detector and data analyses were performed by a large number of CLAS Collaboration members, who also discussed and approved the scientific results. The analysis presented here was performed primarily by I.K with help from A.D. GCF calculations and model systematic uncertainty studies were done by A.D. and A.K with guidance from A.S. and J.R.P. Mean-field spectral function calculations were done by A.L and N.R. O.H., A.S., E. Piasetzky, and L.B.W. initiated, guided and supervised the analysis.

Competing interests The authors declare no competing interests.

Data Availability The raw data from this experiment are archived in Jefferson Lab's mass storage silo.

Author Information Reprints and permissions information is available at www.nature.com/reprints. Readers are welcome to comment on the online version of the paper. Publisher's note: Springer Nature remains neutral with regard to jurisdictional claims in published maps and institutional affiliations. Correspondence and requests for materials should be addressed to O.H. (hen@mit.edu).

Full Author List
xxxx TBD xxxx

Methods

CLAS detector and particle identification. The CEBAF Large Acceptance Spectrometer (CLAS) was based on a toroidal magnetic field and had six independent sectors separated by its magnet coils [22]. Each sector included three layers of drift chambers for charged particle momentum and charge determination, and time-of-flight scintillation counters, Cherenkov counters, and electromagnetic calorimeters for particle identification. The in-plane scattering angle coverage of the drift chambers and time-of-flight scintillation counters extended from about 8° to 140°, while that of the Cherenkov counters and electromagnetic calorimeters was more limited, extending from about 8° to 45°. The six sectors collectively covered $50-80\%$ of the out-of-plane angle (depending on the in-plane scattering angle).

Electrons were distinguished from pions by their signal in the Cherenkov counters, as well as by a large energy deposition in the electromagnetic calorimeters relative to their momentum. Protons were identified by requiring that their time of flight, measured by the scintillation counters, was consistent to within two standard deviations of the timing measurement resolution, with the calculated time of flight based on the momentum reconstructed in the drift chambers. We applied separate fiducial cuts for electrons and protons to select momentum-dependent regions of CLAS where the detection efficiency was constant and close to 100%.

We used a specialized dual target setup intended to enable precise extractions of A/d cross section ratios [21]. The target consisted of a 2-cm long liquid deuterium target, held inside a thin aluminum cell, followed by an insertable thin solid foil of C, Al, Fe, or Pb. The solid foil was placed 4 cm from the end of the liquid deuterium cell, which allowed us to unambiguously identify which particles originated from the electron interaction with the liquid deuterium and which particles originated from the solid target foil. For each event, the measured electron and proton vertices along the beam direction were required to agree to within 0.8 cm, which corresponds to about two standard deviations of the vertex reconstruction resolution.

Event Selection for $(e, e'p)$. We required $Q^2 >$ 1.5 (GeV/c)^2 and $\theta_{pq} \leq 25°$, i.e., that the knocked-out proton be detected within a 25° cone of the momentum transfer vector, $\vec{q}$ [27, 28]. This ensured that the detected proton was the one that absorbed the virtual photon. We also required $350 \leq p_{miss} \leq 600$ MeV/c for the scaling studies, but relaxed that requirement when studying the transition to scaling.

Rather than cutting solely on the missing-mass to select QE contributions and reject inelastic events, we used a loose missing-mass cut and an x_B-dependent cut on $\theta_{\vec{p}_{miss},\vec{q}}$, the angle between $\vec{p}_{miss}$ and $\vec{q}$. The missing mass was defined for an electron scattering from a stationary two-nucleon pair:

$$M^2_{miss} = (\omega + m_d - E_p)^2 - |\vec{q} - \vec{p}_p|^2, \qquad (1)$$

where $E_p = \sqrt{|\vec{p}_p|^2 + m^2}$ is the proton energy and $m_d \approx 2m$ is the deuteron mass. In reality, the two-nucleon pair has a binding energy E^* and a non-zero pair center-of-mass (CM) momentum $\vec{p}_{CM}$, which broadened the missing mass distribution.

Extended Data Fig. 1 shows the measured M_{miss} (see Eq. 1) distribution for ^{12}C$(e, e'p)$ events for different bins of x_B. There is a peak at the nucleon mass due to quasielastic proton knockout and a background at larger missing mass due to inelastic scattering from nucleons resulting in meson production. Since the minimum p_{miss} increases with x_B for $x_B > 1$, at high-x_B, where most previous measurements were done, only QE events are seen. We cut on $0.8 \leq M_{miss} \leq 1.08$ GeV/c$^2 \approx m + m_\pi$ (where m_π is the pion mass), to suppress most inelastic contributions. However, due to broadening, inelastic events extend to lower missing mass and cannot be cleanly separated by a simple cut on M_{miss}. Since the functional form of the inelastic background is not known, fitting the background would lead to very large uncertainties.

Therefore we adopted the method of Ref. [5, 34] and used $\theta_{\vec{p}_{miss},\vec{q}}$, the angle between $\vec{p}_{miss}$ and $\vec{q}$, to separate QE and inelastic events (see Extended Data Fig. 2). In non-QE (inelastic) reactions the momentum transferred to undetected particles shifts the direction of $\vec{p}_{miss}$ and increases $\theta_{\vec{p}_{miss},\vec{q}}$. In contrast to the missing-mass spectra, $\theta_{\vec{p}_{miss},\vec{q}}$ is well described by a two-Gaussian fit. We fit the $\theta_{\vec{p}_{miss},\vec{q}}$ distribution with two Gaussians and selected the cut-off angle between the QE and background events as the point where the two Gaussians intersected. This suppressed the vast majority of the inelastic events while keeping most of the QE events. The contamination due to inelastic events (false positives) was partially balanced by the loss of elastic events (false negatives). In addition, the remaining fractional contribution of the inelastic events in the QE region is similar in both the heavy nuclei and the deuterium spectra and therefore largely cancels in their ratios. As in the M_{miss} spectra, the inelastic peak decreases rapidly as x_B increases above 1.1.

The effect of the $\theta_{\vec{p}_{miss},\vec{q}}$ cut on the missing mass distribution is shown in Extended Data Fig. 1 where the dashed histograms show the missing-mass distributions separately for events above and below the cut. This cut thus identifies the inelastic tail that extends into the QE region. The small-$\theta_{\vec{p}_{miss},\vec{q}}$ events in the M_{miss} distribution are well described by a Gaussian. This is an encouraging observation that shows that our procedure results in similar performance to those of the traditional peak+background fit procedure, but using well defined kinematical cuts that are suitable for QE scattering studies, and allow for direct comparison with theoretical calculations.

To test our identification of QE SRC breakup events we examined the width of the resulting missing-mass peak after the $\theta_{\vec{p}_{miss},\vec{q}}$ cut. The width of this distribution depends on the CLAS resolution and on the SRC pair CM motion. We subtracted the deuterium missing mass peak width (which depends only on the CLAS resolution) from that of the heavier nuclei for each x_B bin in order to determine the intrinsic width due to the pair CM motion, $\sigma^A_{int} = \sqrt{(\sigma^A_{exp})^2 - (\sigma^d_{exp})^2}$, where σ_{exp} is the measured missing mass distribution width extracted from a Gaussian fit to the data.

The resulting x_B dependence of σ^C_{int} (see Extended Data Fig. 3) agrees well with a calculation using the Generalized Contact Formalism (GCF) [10, 20, 29] that assumes electron scattering from nucleons in SRC pairs with a realistic Gaussian CM momentum distribution [35], as was done in Refs. [28, 30, 31]. The calculation accounts for the CLAS detector acceptance and resolution and our event selection cuts. The width of the CM momentum distributions, σ_{CM}, and the excitation energy of the residual nuclear system after the SRC breakup, E^*, were determined from fits to the data. The fitted values of σ_{CM} (68% and 90% confidence ranges of $160-210$ MeV/c and $125-220$ MeV/c, respectively) agree well with previous direct measurements [31, 35]. While E^* was not previously measured, the resulting 68% and 90% confidence ranges of $20-55$ MeV and $0-70$ MeV are consistent with previous analyses [28]. The sensible values of the resulting fit parameters and the agreement between the GCF calculation and the data further support our interpretation of the data as dominated by scattering off SRC pairs.

We varied the $\theta_{\vec{p}_{miss},\vec{q}}$ cut to show that our results are not sensitive to the specific method of removing the inelastic contributions (see Extended Data Fig. 6). Varying the angular cut by $\pm5°$ and even removing it entirely did not significantly change the cross section ratios. This shows that the effect of the residual inelastic contributions largely cancels in the cross section ratio.

The systematic uncertainties associated with our event selection cuts, including the inelastic suppression cuts, are discussed below.

Cross section extraction. The reported per-nucleon cross section ratios were extracted from the measured number of $(e,e'p)$ events originating from the solid and liquid deuterium targets by normalizing them by the integrated measured per-nucleon luminosity, and applying corrections for experimental effects such as acceptance and electron radiative effects, as well as for nucleon attenuation effects. The general expression for the per-nucleon $(e,e'p)$ A/d cross section ratio for a given x_B bin is given by:

$$\frac{\sigma_A/A}{\sigma_d/2}(x_B) = \frac{Y^A_{(e,e'p)}(x_B)}{Y^d_{(e,e'p)}(x_B)} \times Acc_{A/d}(x_B) \times RC_{A/d}(x_B) \times \frac{T_d}{T_A}, \tag{2}$$

where $Y^A_{(e,e'p)}(x_B)$ and $Y^d_{(e,e'p)}(x_B)$ are the measured number of $(e,e'p)$ events from target A or d, respectively, in a given x_B bin normalized by luminosity, $Acc_{A/d}(x_B)$ is the relative acceptance of the CLAS detector for $(e,e'p)$ events originating from the solid foil target relative to those from the liquid deuterium target, $RC_{A/d}(x_B)$ is the ratio of the nucleus A and d radiative correction factors, and T_A and T_d are transparency factors accounting for the attenuation of nucleons as they exit nucleus A or nucleus d.

Deuteron yield. To determine the deuteron event yield, $Y^d_{(e,e'p)}(x_B)$, we separated events originating from interactions with deuterium nuclei and with the aluminum end caps of the target cell. We minimized the end cap contributions by only considering events with an interaction vertex reconstructed to within the central 1 cm of the 2-cm liquid target. We then used measurements with an empty target cell to estimate the remaining cell wall contributions. These contributions were independent of x_B and less than 2% of the measured event yield. We thus reduced the measured yield by 2% and accounted for the uncertainty in this subtraction in our systematic uncertainties.

Acceptance Corrections. We corrected the cross section ratio for the slightly different experimental acceptances for events originating in the 2-cm liquid deuterium target and events originating in the solid target foil located 5-cm downstream from the liquid target center. This factor should be small because the target separation is much smaller than the distances from the targets to the detectors. We estimated this correction factor using a Geant simulation of CLAS [32]. We generated separate acceptance maps for electrons and for protons originating from a solid target or from the liquid target as a function of particle momentum and in- and out-of-plane scattering angles. We then used the acceptance maps to calculate the acceptance probability for each experimental event as follows. For each event, we rotated the entire event (both electron and proton) by a random angle ϕ around the beamline and then rotated the proton momentum by a random angle ϕ' around $\vec{q}$. We then used the acceptance maps to determined the probability that the rotated event, which has approximately the same cross section as the measured event, would have been detected by CLAS. We did this calculation separately for events from the liquid and solid targets, accounting for the target position when constructing the acceptance maps. This procedure was repeated 100 times for each event. The acceptance weight for that event equalled 100 divided by the total probability that each of those 100 rotated events would have been detected. The average acceptance weight as a function of x_B for each target is shown in Extended Data Fig. 7(a). We then took the ratios between the solid- and liquid target acceptance weights to determine $Acc_{A/d}(x_B)$, the cross section ratio acceptance-correction factor for each x_B-bin (see Extended Data Fig. 7). The uncertainties in $Acc_{A/d}(x_B)$ were added in quadrature to the point-to-point statistical uncertainties of the data.

Radiative and Coulomb effects. The radiative correction factors were determined by calculating the ratio between the Born cross section and the cross section including electron-radiative effects. The latter uses the peaking approximation [36] as implemented in Ref. [30]. The cross sections for the solid targets were calculated using the GCF model and the deuteron cross sections were calculated with the AV18 momentum distribution, as described below. As part of the modified electron kinematics, we also used the Effective Momentum Approximation [37] to account for Coulomb effects that accelerate the incoming electron and knockout proton and decelerate the scattered electron by an energy ΔE, see Ref. [30] for details. We used ΔE values of 0, 2.9, 5.6, 9.4 and 20.3 MeV for d, C, Al, Fe and Pb targets, respectively. The resulting radiative correction factors, $RC_{A/d}(x_B)$, are shown in Extended Data Fig. 8.

Transparency Corrections. After the electron scatters from a proton, the proton needs to travel through the residual nucleus to be detected. If the proton rescatters too much from the other nucleons, then it will fall outside our event acceptance cuts. The probability of the proton to be detectable after exiting from the nucleus depends on the size of the nucleus. The nuclear transparency probabilities were calculated within a Glauber approximation using an effective scattering cross section. The probability that a proton escapes the nucleus without further interaction is given by:

$$T_A = \frac{1}{A}\int d^3r\rho(r)\exp\left[-\sigma_{eff}\int\rho(z)dz\right], \qquad (3)$$

where $\rho(r)$ is the nuclear density distribution (assumed symmetrical), $\rho(z)$ is the nuclear density along the path of the exiting proton, and σ_{eff} is the effective nucleon-nucleon cross section. For the $1-3$ GeV/c protons in this analysis, $\sigma_{eff} = 37\pm 7$ mb. This gives nuclear transparencies T_A of $1, 0.53\pm 0.05, 0.43\pm 0.05, 0.34\pm 0.04$ and 0.22 ± 0.03 for d, C, Al, Fe and Pb, respectively.

Theoretical cross section calculations. The $(e,e'p)$ nucleon-knockout cross section for high-Q^2 reactions is modeled here using a factorized plane wave impulse approximation (PWIA) [38]:

$$\frac{d\sigma_{A(e,e'p)}}{d\Omega_{k'}dE_{k'}d\Omega_p dE_p} = p_p E_p \sigma_{ep} S_A^N(p_{miss}, E_{miss}), \qquad (4)$$

where $(\vec{k}', E_{k'})$ is the scattered electron four-momentum, σ_{ep} is the off-shell electron-nucleon cross section, and $S_A^N(p_{miss}, E_{miss})$ is the nuclear spectral function for nucleus A, which defines the probability for finding a nucleon in the nucleus with momentum p_{miss} and energy E_{miss} (in the following for brevity we drop the "miss" subscript):

$$S_A^N(\mathbf{p}, E) = \sum_n |\langle\Psi_0^A|[|p\rangle\,|\Psi_n^{A-1}\rangle]|^2 \times \delta(E + E_0^A - E_n^{A-1}). \qquad (5)$$

where $|p\rangle$ is the single-nucleon state, $|\Psi_0^A\rangle$ is the ground state of the Hamiltonian with energy E_0, whereas $|\Psi_n^{A-1}\rangle$ and E_n^{A-1} are the energy eigenstates and eigenvalues of the $(A-1)$-nucleon system. Note that the single-nucleon momentum distribution is recovered by integrating the spectral function over the removal energy $n_A^N(\mathbf{p}) = \int dE S_A^N(\mathbf{p}, E)$.

From the above relations, it is clear the deuterium spectral function equals the momentum distribution times a delta function in missing energy. To construct it, we used the AV18 deuterium momentum distribution from Ref. [39].

For nuclei with $A > 2$, we considered two models for spectral function, for the mean-field and for the SRC region. The mean-field component $S_N^{MF}(\mathbf{p}, E)$ corresponds to restricting the sum of Eq. (5) to the bound $A-1$ states

$$S_A^{N,MF}(\mathbf{p}, E) = \sum_n |\langle\Psi_0^A|[|p\rangle\otimes|\Psi_n^{A-1}\rangle]|^2 \times \delta\Big(E - B_0^A + B_n^{A-1} - \frac{\mathbf{p}^2}{2m_n^{A-1}}\Big), \qquad (6)$$

where B_0^A and B_n^{A-1} are the binding energies of the initial and the $A-1$ remnant nucleus left in a state n with mass m_n^{A-1}. The p-shell momentum-space overlaps $\langle\Psi_0^A|[|p\rangle\otimes|\Psi_n^{A-1}\rangle$ are computed by Fourier transforming the variational Monte Carlo (VMC) radial overlaps for the transitions [40]:

$$^{12}\mathrm{C}(0^+) \to {}^{11}\mathrm{B}(3/2^-) + p$$
$$^{12}\mathrm{C}(0^+) \to {}^{11}\mathrm{B}(1/2^-) + p$$
$$^{12}\mathrm{C}(0^+) \to {}^{11}\mathrm{B}(3/2^-)^* + p\,.$$

The quenching of the spectroscopic factors (i.e. the de-occupancy of shell model orbitals due to many body correlations) automatically emerges from the VMC calculations, as they encompass multi-nucleon correlations generated by the highly-realistic AV18 + UX Hamiltonian [41]. This calculation is not available for heavier nuclei.

Computing the s-shell mean-field contribution would in principle require evaluating the spectroscopic overlaps for the transitions $^{12}\mathrm{C}(0^+) \to {}^{11}\mathrm{B}(1/2^+)^* + p$ for all the possible excited states of ^{11}B with $J^P = (1/2^+)$. This procedure involves non-trivial difficulties for the VMC method, which is best suited to study ground-state properties. To circumvent them, we model the s-wave single-particle orbitals using harmonic oscillator and Woods-Saxon one-body potentials. We adjust the value of the oscillator frequency $\hbar\omega$ and the parameters of the Wood-Saxon potential so that the Fourier transform of the (quenched) p-wave orbitals reproduce that of the VMC. The quenching factor of the s-wave orbital is fixed to reproduce the integrated strength of the VMC momentum distribution up to k_F. As an alternative strategy, we also calculated the VMC overlap associated with the $^4\mathrm{He}(0^+) \to ^3\mathrm{H}(1/2^+) + p$ transition. Since nuclear correlation effects are already included in this VMC overlap, only minimal changes to the quenching factor are needed to reproduce the integral of the momentum distribution up to k_F. As shown in Extended Data Fig. 9, the VMC total momentum distribution agrees well with the ones computed by adding the VMC p-wave overlap and the s-shell overlap obtained from the harmonic oscillator (HO), Wood Saxon (WS) and $^4\mathrm{He}(0^+) \to ^3\mathrm{H}(1/2^+) + p$ calculations.

We constructed the spectral-function energy dependence using the experimental values for the binding energies of the ground state of ^{12}C and for the states $^{11}\mathrm{B}(3/2^-)$, $^{11}\mathrm{B}(1/2^-)$, and $^{11}\mathrm{B}(3/2^-)^*$. The energy conserving δ-function of Eq. (5) is parametrized using a narrow Gaussian distribution whose widths are fixed so as to reproduce the missing energy spectra of the $(e, e'p)$ data of Ref. [42]. This data set has also been used to determine the energy centroid and width for the $^{12}\mathrm{C}(0^+) \to ^{11}\mathrm{B}(1/2^+)^* + p$ s-shell transition. Note that the mean-field spectral function already accounts for the reduced occupancy of mean-field states due to multi-nucleon correlations, as the normalization of the spectroscopic overlaps is fixed by VMC calculations. Since the integral is fixed, changing the width of the Gaussian distributions changes the peak heights in the missing-energy spectral function. We varied the widths by 10% to determine the dependence of the results on the widths. We used the cross section variation due to using the different s-shell calculations as an uncertainty for the orange band in Fig. 3a.

The SRC spectral functions for C, Al, Fe and Pb were modeled using the GCF model [10, 20, 29] following the implementation of Ref. [30] with the AV18 two-nucleon interaction, using pair CM motion width of 150 ± 20 MeV/c, and an $A - 2$ excitation energy of $0 - 30$ MeV. The contacts (the probability of finding an SRC pair) were taken from [10].

The complete deuterium spectral function was calculated exactly using the AV18 nucleon-nucleon interaction [39].

The calculated cross sections were integrated over the CLAS experimental acceptance, using the same event selection cuts as the data, and smeared to account for the CLAS experimental resolution.

Systematic Uncertainties. There were several sources of systematic uncertainties, including both point-to-point and correlated uncertainties.

Coulomb Correction: There is a 10% uncertainty in the Coulomb potential (ΔE) used for the Coulomb correction described above. Varying ΔE by $\pm 10\%$ changed the extracted cross section ratios by a maximum of 3% (for lead). We conservatively chose to use 3% as the point-to-point systematic uncertainty due to Coulomb correction for all targets and all bins.

Event Selection: We varied each of the event selection cuts within reasonable limits (see Extended Data Table 1) to see the effect of these cuts on the resulting cross section ratios. We repeated the analysis 100 times, choosing the value of each selection cut randomly from a Gaussian distribution centered at the nominal value with a width reflecting a reasonable variation of the cut. We used the mean and variance in the resulting distribution of 100 cross section ratios to define the value of cross section ratio and its event selection cut uncertainty, respectively. These bin-dependent (point-to-point) uncertainties ranged from 4.5% to 12.5%.

Inelastic Background Rejection: We varied the $\theta_{\vec{p}_{miss},\vec{q}}$ cut by $\pm 5°$ to see the effect of the differential inelastic background on the cross section ratios (see Extended Data Fig. 6). We added a point-to-point systematic uncertainty equal to the cross section ratio difference between the $+5°$ and $-5°$ cuts divided by $\sqrt{12}$.

Transparency: The largest normalization systematic uncertainty is due to the transparency correction. It is driven by the uncertainties in the effective nucleon scattering cross sections used for the Glauber calculations that result in 10% (for carbon) to 15% (for lead) uncertainties in the ratios of transparencies of the solid target nuclei to deuterium, see Ref. [27].

Combining different deuteron run periods: We measured electron scattering from deuterium and from each solid target simultaneously. In order to increase the deuterium statistics, we combined the deuterium data from all of the solid target runs. This reduced the statistical uncertainty of the cross section ratios but introduced a systematic uncertainty due to the stability of the beam charge measurement that does not fully cancel in the A/d cross section ratio. This uncertainty was estimated as half of the difference between the total averaged and the individual deuteron normalized yields. The maximum difference was 1.5%, which we used as a normalization systematic uncertainty.

Inclusive Scaling Measurements. Previous scaling studies identified scattering from high-momentum nucleons by measuring the inclusive (e, e') reactions at large Q^2 and x_B. For a given x_B and Q^2, there is a minimum nucleon momentum for absorbing the virtual photon. This minimum momentum increases with x_B. It also depends on whether the missing momentum is carried by one other nucleon (for scattering from the deuteron or from a nucleon in an SRC pair) or by the other $A-1$ nucleons of the residual nucleus (for scattering from a mean-field nucleon) [24].

For $Q^2 \geq 1.5$ GeV/c^2, the cross section ratio of nuclei to deuterium is independent of x_B for $1.5 \leq x_B \leq 1.9$ [15, 17, 24–26], a phenomena we call scaling (see Figs. 2 and 1). The value of the cross section ratio in the scaling region is interpreted as a measure of the relative number of nucleons in SRC pairs in the measured nuclei. These inclusive studies also determined the onset of scaling to be 275 ± 25 MeV/c [15] from $x_B = 1.5 \pm 0.05$ at $Q^2 = 1.4$ GeV^2, where scaling starts. This is somewhat larger than the Carbon Fermi momentum and consistent with our results.

However, recent studies [43] show that the relation between Q^2, x_B, and the minimal initial nucleon momentum also depends on the detailed characteristics of SRC pairs, such as their center-of-mass (CM) motion and the excitation energy of the residual nuclear system. This prevents a precise determination of the SRC scaling onset from the high-x_B (e, e') scaling measurements.

In contrast, the $(e, e'p)$ reaction used in this paper is insensitive to such model details since detecting the proton allows us to directly determine $\vec{p}_{miss}$ for each event, thereby enabling a complementary and precise determination of the SRC scaling onset.

Extended Data Table I. Event selection cut ranges

Cut Type	Nominal Value	1σ
p_{miss} minimum [GeV/c]	0.3	0.015
p_{miss} maximum [GeV/c]	0.6	0.015
M_{miss} minimum [GeV/c^2]	0.8	0.05
M_{miss} maximum [GeV/c^2]	1.08	0.05
θ_{pq}	25°	0.5°
Q^2 [(GeV/c)^2]	1.5	0.01

Extended Data

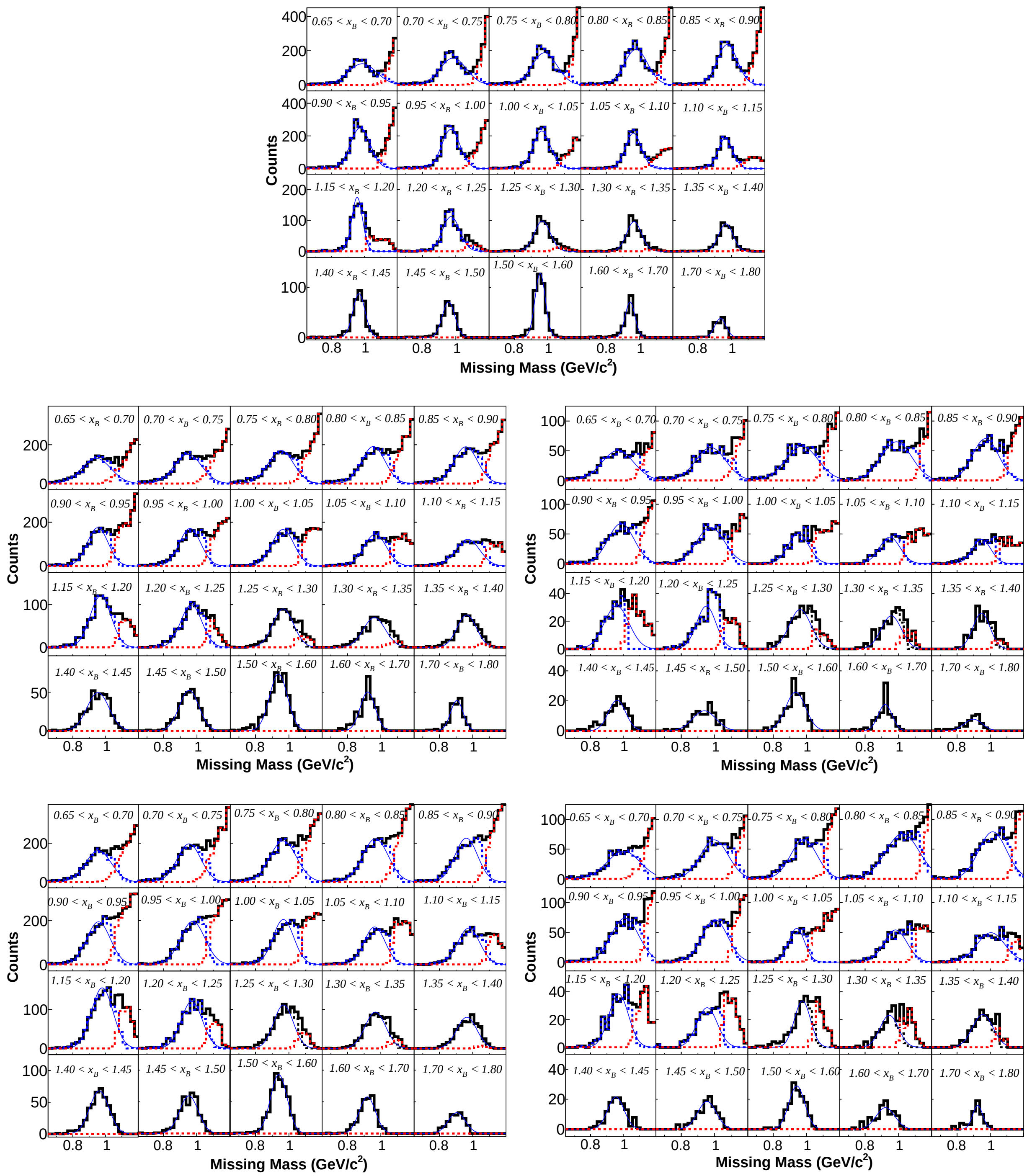

Extended Data Fig. 1. | **Missing Mass distributions.** Number of events plotted vs. M_{miss} for the $(e,e'p)$ reaction for different bins of x_B for D (top), C (middle left), Al (middle right), Fe (bottom left), and Pb (bottom right). The data were cut on $Q^2 \geq 1.5$ GeV^2, $\theta_{pq} \leq 25^\circ$, and $350 \leq p_{miss} \leq 600$ MeV/c. The black histogram represents all events. The blue dashed histogram shows the data cut on $\theta_{\vec{p}_{miss},\vec{q}}$, the opening angle between the missing momentum $\vec{p}_{miss}$ and the virtual photon $\vec{q}$, as determined in Extended Data Fig. 2. The red dashed histogram shows the events failing the $\theta_{\vec{p}_{miss},\vec{q}}$ cut. The thin solid blue line shows the Gaussian fit to the blue dashed histogram.

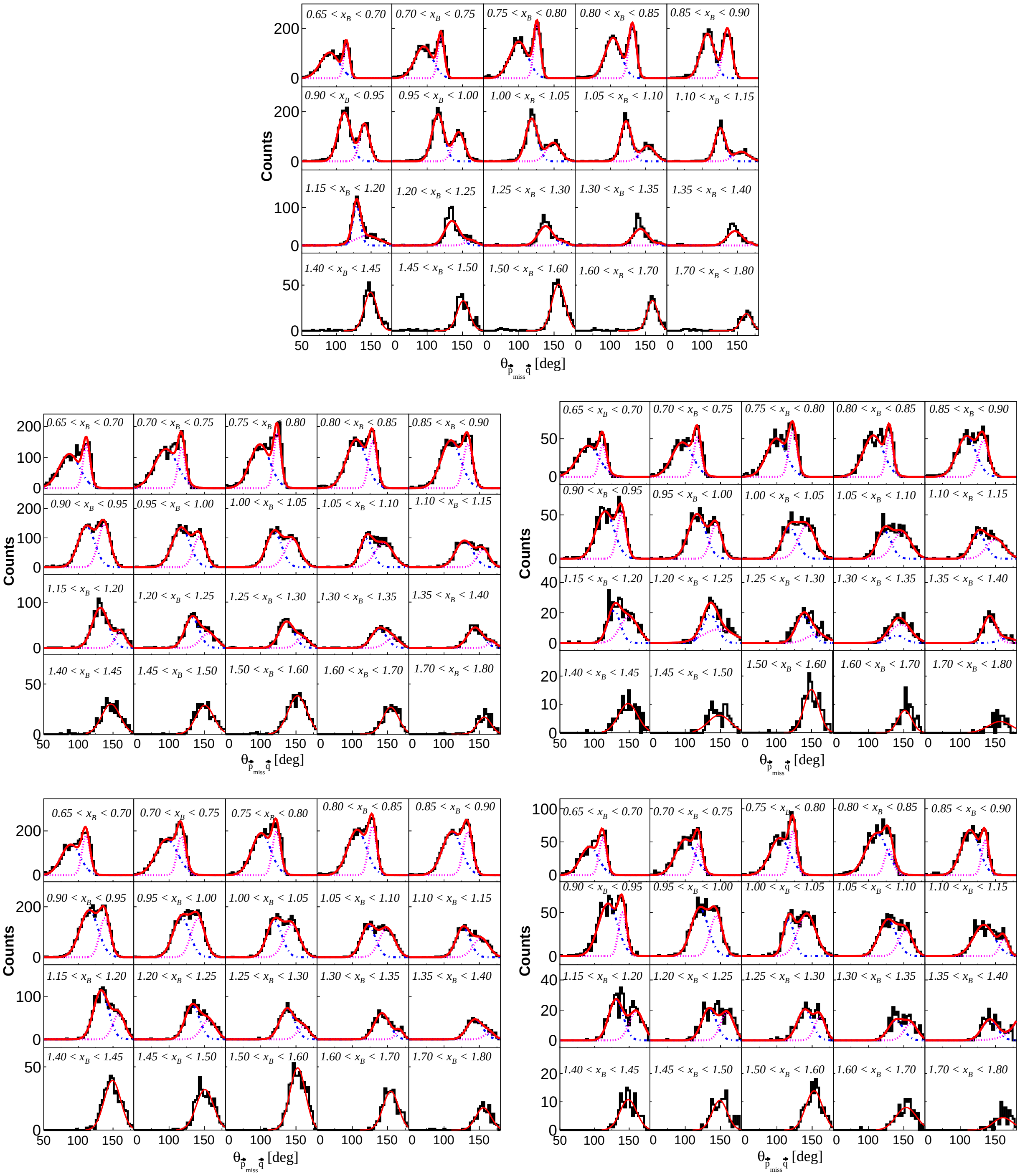

Extended Data Fig. 2. | Opening angle between the missing momentum and the virtual photon. The number of $(e, e'p)$ events plotted vs. $\theta_{\vec{p}_{miss},\vec{q}}$, the opening angle between $\vec{p}_{miss}$ and $\vec{q}$, for different bins in x_B for D (top), C (middle left), Al (middle right), Fe (bottom left) and Pb (bottom right). The data were cut on $Q^2 \geq 1.5$ GeV^2, $\theta_{pq} \leq 25°$, and $350 \leq p_{miss} \leq 600$ MeV/c. The black histogram shows all events, the blue dot-dashed curve and the magenta dotted curves show the Gaussian fits to the two peaks and the total is shown by the solid red line. The intersection of the two Gaussians is used as the angular cut for the dashed histograms in Extended Data Fig. 1. At $x_B \geq 1.4$ only one Gaussian is fit to the data because the inelastic contribution is negligible.

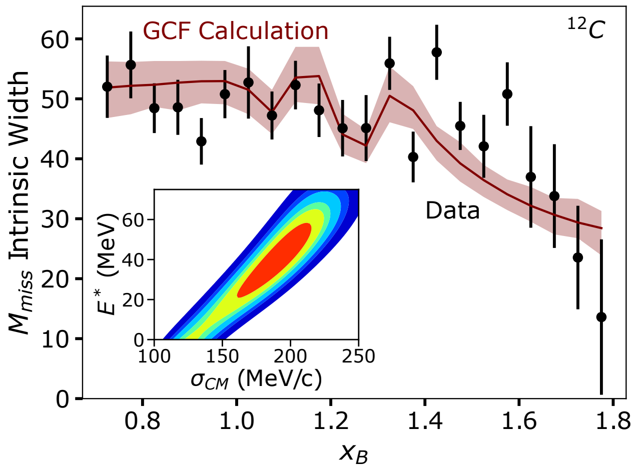

Extended Data Fig. 3. | SRC pair characteristics from $(e, e'p)$ missing mass. The intrinsic width of the ^{12}C missing mass (M_{miss}) distribution, plotted vs x_B. Black points show the data. The red curve and uncertainty band shows an SRC based Generalized Contact Formalism (GCF) calculation [10, 30]. The two main model parameters of the calculation, namely SRC pair CM momentum distribution width σ_{CM} and the residual $A-2$ system excitation energy E^*, are fit to the data. Data error bars and calculation error band show the total uncertainty (statistical + systematical) at the 1σ or 68% confidence level. Inset: The resulting confidence intervals of the correlation between the fitted values of σ_{CM} and E^*. The inner region (red) shows the 1σ (68%) confidence region with each region increasing the confidence by an additional 1σ. The observed agreement between the data and GCF calculation, and the agreement of the fitted model parameters with previous extractions, show the measured $(e, e'p)$ events are consistent with resulting from the hard breakup of SRC pairs.

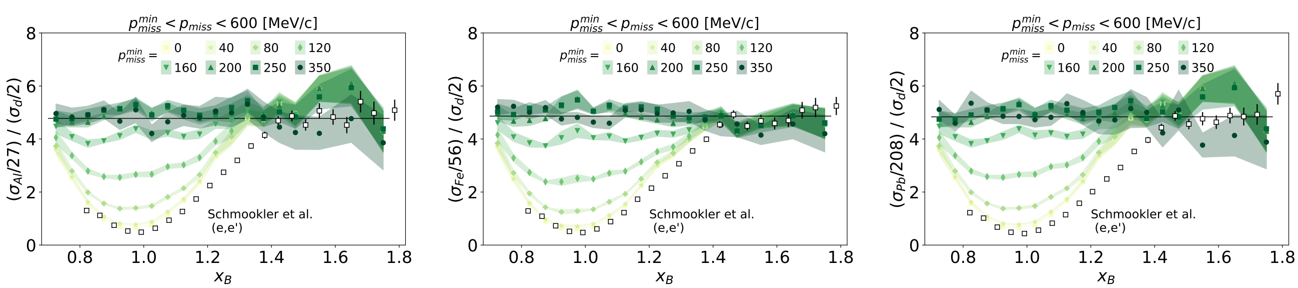

Extended Data Fig. 4. | Scaling development in nuclei-to-deuterium $(e, e'p)$ cross section ratios. The per-nucleon cross section ratios for Al, Fe, and Pb to deuterium as a function of x_B. Full symbols with different colors stand for different lower limits of the missing momentum integration. The upper missing momentum limit is fixed at 600 MeV/c. The colored bands mark the statistical plus point-to-point systematical uncertainty of the data at the $\pm 1\sigma$ or 68% confidence level. Overall systematic uncertainties of 10% (C) to 15% (Pb) are not shown. Open squares are the previously measured inclusive (e, e') per nucleon cross section ratios of Ref. [26]. The horizontal line shows the average (e, e') cross section ratio for $1.45 \leq x_B \leq 1.8$ [26].

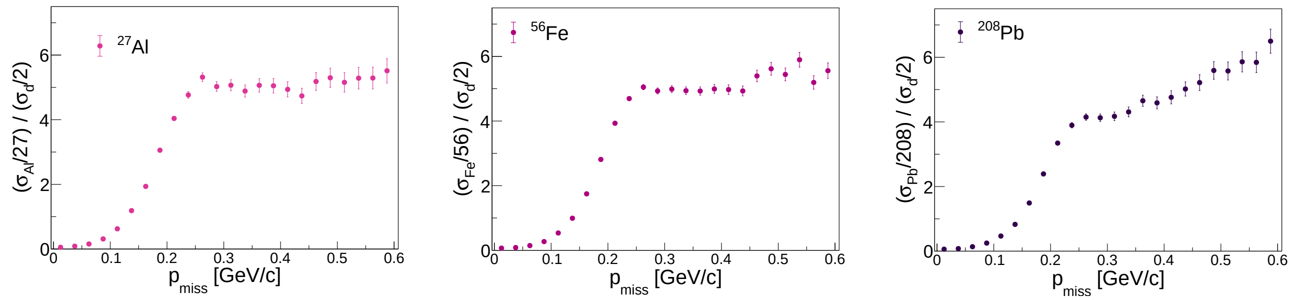

Extended Data Fig. 5. | **Missing momentum scaling.** The per nucleon $(e, e'p)$ cross section ratios for Al (left), Fe (middle), and Pb (right) over deuterium as a function of p_{miss}, integrated over $0.7 \leq x_B \leq 1.8$. The filled blue circles show the data. Data error bars show their uncertainties (statistical plus point-to-point systematical) at the 1σ or 68% confidence level. Overall systematic uncertainty of 10% (C) to 15% (Pb) are not shown.

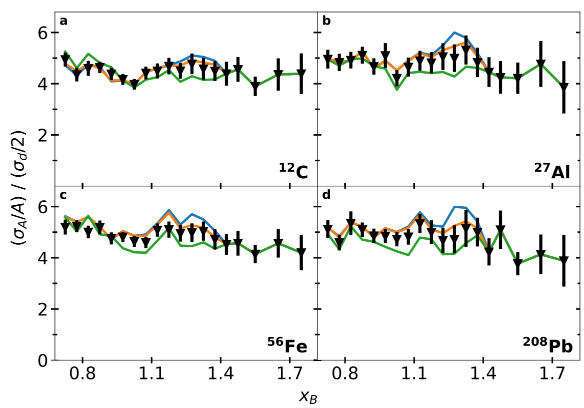

Extended Data Fig. 6. | **Angle cut sensitivity.** Measured per-nucleon cross section ratios for carbon to deuterium with different cuts on $\theta_{\vec{p}_{miss},\vec{q}}$. The black points correspond to the nominal cut values, the green and orange lines show the effect of increasing or decreasing the cut by 5°, respectively, and the blue line shows the effect of not applying any $\theta_{\vec{p}_{miss},\vec{q}}$ cut.

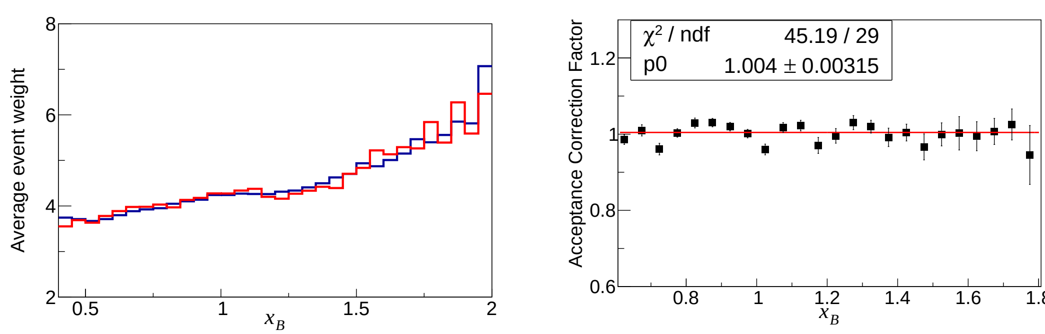

Extended Data Fig. 7. | **Acceptance correction.** (left) The average acceptance weight for $(e, e'p)$ events from the solid (blue histogram) and deuterium (red histogram) targets as a function of x_B and (right) the acceptance correction factors for the cross section ratios, i.e., the ratio of deuterium- to solid-target acceptance-correction weights, as a function of x_B. The points show the data and the error bars show the 1σ or 68% confidence limits. The red line shows a constant fit to the data.

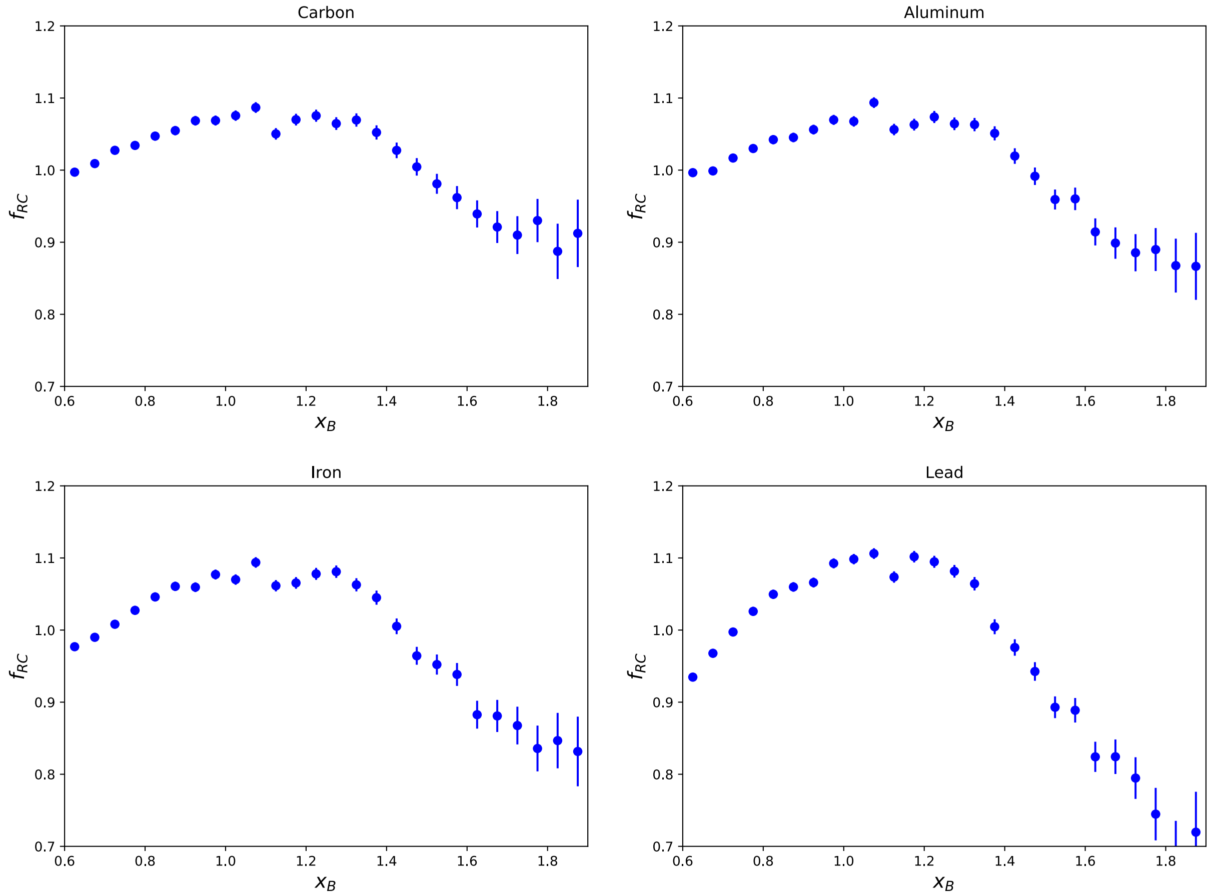

Extended Data Fig. 8. | **Radiative and coulomb corrections.** The combined radiative and Coulomb corrections, $RC_{A/d}(x_B)$, for $(e, e'p)$ events for nucleus A relative to the deuteron for (a) carbon, (b) aluminum, (c) iron, and (d) lead. The points show the correction factors and the error bars show the 1σ or 68% confidence limits.

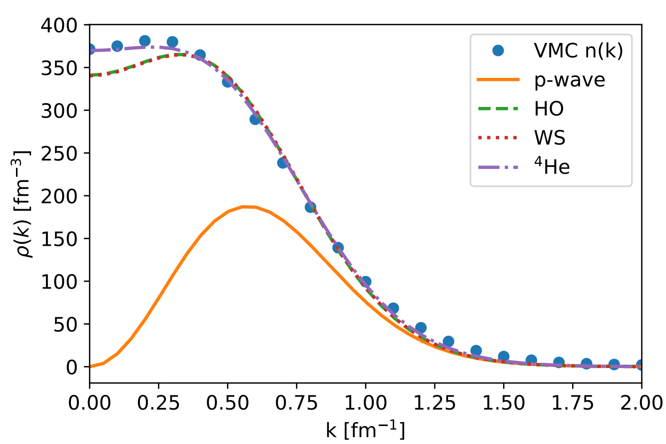

Extended Data Fig. 9. | **Calculated nucleon momentum distributions in ^{12}C.** The filled blue circles represent the total momentum distribution $n(k)$ of ^{12}C computed within the VMC method. The solid orange line shows the sum of the p-wave overlaps between the ^{12}C and ^{11}B+p VMC wave functions. The momentum distributions obtained by adding to the p-wave overlaps the different prescription for the s-wave contribution are displayed by the green dashed line (harmonic oscillator), dotted red line (Wood-Saxon) and dash-dotted purple line (s-wave overlaps between ^{4}He and the ^{3}H+p VMC wave functions). The high-momentum contributions of long- and short-range correlations are not visible on this linear scale.